J. Fluid Mech. (2007), *vol.* 582, *pp.* 253–280.
doi:10.1017/S0022112007005848 Printed in the United Kingdom

Direct numerical simulation of stenotic flows. Part 1. Steady flow

SONU S. VARGHESE[1], STEVEN H. FRANKEL[1] AND PAUL F. FISCHER[2]

[1]School of Mechanical Engineering, Purdue University, 585 Purdue Mall, West Lafayette, IN 47907, USA

[2]Mathematics and Computer Science Division, Argonne National Laboratory, Argonne, IL 60439, USA

(Received 29 January 2005 and in revised form 16 January 2007)

Direct numerical simulations (DNS) of steady and pulsatile flow through 75 % (by area reduction) stenosed tubes have been performed, with the motivation of understanding the biofluid dynamics of actual stenosed arteries. The spectral-element method, providing geometric flexibility and high-order spectral accuracy, was employed for the simulations. The steady flow results are examined here while the pulsatile flow analysis is dealt with in Part 2 of this study. At inlet Reynolds numbers of 500 and 1000, DNS predict a laminar flow field downstream of an axisymmetric stenosis and comparison to previous experiments show good agreement in the immediate post-stenotic region. The introduction of a geometric perturbation within the current model, in the form of a stenosis eccentricity that was 5 % of the main vessel diameter at the throat, resulted in breaking of the symmetry of the post-stenotic flow field by causing the jet to deflect towards the side of the eccentricity and, at a high enough Reynolds number of 1000, jet breakdown occurred in the downstream region. The flow transitioned to turbulence about five diameters away from the stenosis, with velocity spectra taking on a broadband nature, acquiring a $-5/3$ slope that is typical of turbulent flows. Transition was accomplished by the breaking up of streamwise, hairpin vortices into a localized turbulent spot, reminiscent of the turbulent puff observed in pipe flow transition, within which r.m.s. velocity and turbulent energy levels were highest. Turbulent fluctuations and energy levels rapidly decayed beyond this region and flow relaminarized. The acceleration of the fluid through the stenosis resulted in wall shear stress (WSS) magnitudes that exceeded upstream levels by more than a factor of 30 but low WSS levels accompanied the flow separation zones that formed immediately downstream of the stenosis. Transition to turbulence in the case of the eccentric stenosis was found to be manifested as large temporal and spatial gradients of shear stress, with significant axial and circumferential variations in instantaneous WSS.

1. Introduction

Atherosclerosis, a cardiovascular disease of the larger arteries, is the primary cause of heart disease and stroke. In the United States alone, statistics released by the American Heart Association estimated that more than 70 million Americans have one or more forms of cardiovascular disease, with coronary heart disease being the single leading cause of death, claiming almost 20 % of all deaths in 2002. Atherosclerosis is a progressive disease initiated by localized fatty streak lesions within the arteries

occurring as early as childhood. Over decades, these lesions can develop into more complex plaques large enough to significantly block blood flow within the circulatory system (Lusis 2000). This local restriction of the artery is known as an arterial stenosis. Plaque deposition is most common in the aorta, coronary arteries, and carotid arteries; and, as one might expect, the presence of a stenosis can lead to serious health risks. Stenoses are commonly characterized as a percentage reduction in diameter or area of the host vessel and are considered clinically significant when the reduction is greater than 75 % by area (Young 1979; Ku 1997). The progression of a low-level arterial blockage into a critical stenosis is in itself the result of complex nonlinear interactions between factors such as flow conditions, wall compliance, and biological responses (Berger & Jou 2000).

The cardiovascular system typically features low-Reynolds-number pulsatile flow due to the cyclic pumping motion of the heart. In particular, stenotic flows may feature flow separation, recirculation, and reattachment, as well as strong shear layers that, when combined with flow pulsatility, can result in periodic transition to turbulence in the post-stenotic region. Thus, the presence of a critical stenosis can reduce the flow rate through non-recoverable head loss and flow choking. For example, a stenosis in one of the major vessels supplying the brain can choke the flow and lead to a cerebral stroke (Young 1979). The larger velocities at the stenosis as the flow accelerates through the occlusion lead to high shear stresses at the stenosis throat (or neck) which can activate platelet accumulation and induce thrombosis, leading to plaque rupture and complete blockage of the vessel. Low, oscillatory shear stresses in the disturbed flow regions have been directly implicated in the progression of arterial wall thickening and atherosclerotic disease (Ku 1997; Wootton & Ku 1999). Understanding the complex flow features that occur in the vicinity of a stenosis is thus critical to understanding the possible mechanisms by which induced flow dynamics can contribute to disease progression.

1.1. *Pulsatile turbulent wall-bounded flow*

In the most idealized sense, a stenosed vessel resembles a straight rigid pipe with a constriction. A number of works have focused on the topic of unsteady turbulent pipe flows, including periodic pulsating flows and non-periodic transient flows. The fundamental variables involved in pulsatile flows are the amplitude and frequency of the pulsatile wave and the mean flow rate. Several studies have shown that the effect of amplitude on velocity and turbulence is small, while that of the pulsating frequency and mean flow rate can be significant (He & Jackson 2000).

Winter & Nerem (1984) reviewed pulsatile flows and qualitatively classified them into three types: (*a*) laminar flow, which exists throughout the cycle with no disturbances at any time; (*b*) periodic generation of turbulence, which arises when high-frequency velocity fluctuations appear at the beginning of the decelerating phase of the flow cycle, decrease in intensity as mean flow velocity decreases, and dissipate as the flow relaminarizes at the beginning of the subsequent acceleration phase; and (*c*) fully turbulent flow, which occurs throughout the cycle. More recently, He & Jackson (2000) provided a thorough review of the literature dealing with turbulence in transient pipe flow. Their study of the same subject yielded valuable insight into some fundamental aspects of turbulence dynamics. They observed that turbulence intensity is attenuated in accelerating flows and increased in decelerating flows mainly because of the delayed response of turbulence production, a delay in turbulent energy redistribution among its three components, and a delay associated with the radial propagation of turbulence.

Scotti & Piomelli (2001*a*) conducted direct numerical simulations (DNS) and large-eddy simulations (LES) of pulsating flow in a channel at different frequencies and examined the time-dependent characteristics of the flow as well as the distribution of instantaneous coherent structures, which were found to be phase dependent. At low frequencies, more relevant for the physiologic flows motivating the present study, the flow contained very little turbulent kinetic energy at the beginning of the acceleration phase but eventually developed long smooth streaks that burst into a turbulent spot towards the end of acceleration. The localized spot was found to spread to the entire flow during the deceleration phase. Scotti & Piomelli (2001*b*) also employed the Reynolds-averaged Navier–Stokes (RANS) equations to assess the capabilities of different turbulence models in predicting the same flow. The RANS approach involves computation of only the mean flow, with the effects of the turbulent eddies being modelled. The velocity profiles computed by the turbulence models over the course of a cycle agreed well with the DNS and LES profiles, but differences in other turbulence quantities were noted.

1.2. *Experimental stenotic flow studies*

Because of the obvious limitations of conducting *in vivo* measurements of flow in stenosed arterial vessels, several *in vitro* studies have been performed to study the post-stenotic flow field. In a majority of these studies, factors such as wall compliance, non-Newtonian fluid behaviour, and the constituent particles in blood have been neglected, being regarded as of secondary importance in most physiological stenotic flows (Ku 1997).

Giddens and coworkers have made extensive laser Doppler anemometry measurements of stenotic flows using Plexiglas models of axisymmetric stenotic vessels, under conditions of both steady and pulsatile inflow (Cassanova & Giddens 1978; Deshpande & Giddens 1980; Khalifa & Giddens 1981; Ahmed & Giddens 1983*a*, *b*, 1984; Lieber & Giddens 1988, 1990). For steady flow at low Reynolds numbers of about 500, the post-stenotic flow field contained only disturbances associated with discrete-frequency vortex shedding. Transition to turbulence was restricted to models with a stenosis degree higher than 75 % (by area), at Reynolds numbers greater than 1000 (Ahmed & Giddens 1983*a*, *b*). In the case of pulsatile flow at a physiologically relevant mean (cycle-averaged) inlet Reynolds number of 600, a start-up coherent vortex structure was produced at the beginning of each cycle and was accompanied by discrete-frequency laminar oscillations that amplified during the early stages of flow deceleration in the immediate post-stenotic region; but the flow remained stable for mild constrictions of degree 50 % or less. For the clinically significant 75 % stenosis, unstable discrete-frequency velocity oscillations evolved into turbulence during the deceleration phase and interacted with the starting structure (Ahmed & Giddens 1984). From here on, all stenosis degrees are expressed in terms of percentage area reduction.

In a later work, Ojha *et al.* (1989) studied pulsatile flow through constricted tubes using photochromic tracer methods. They observed that with occlusions of less than 50 %, isolated regions of vortical structures were found in the vicinity of the reattachment point, primarily during the deceleration phase. For tighter constrictions, transition to turbulence was triggered just prior to peak flow, attributed to the breakdown of streamwise vortices shed in the shear layer. Other noteworthy experimental studies of stenotic flows within the past three decades include the work of Kim & Corcoran (1974), Fredberg (1974), Young & Tsai (1979*a*, *b*), Clark (1980), Lu, Gross & Hwang (1980), Lu, Hui & Hwang (1983), and Abdallah & Hwang (1988).

1.3. *Computational modelling of stenotic flows*

In the past decade or so, computational fluid dynamics (CFD) has begun to play a major role in studying arterial flows, and stenotic flows in particular. CFD studies have considered both steady and pulsatile stenotic flows, coupled with fluid–structure interactions, non-Newtonian effects, and flow in geometries reconstructed from clinical magnetic resonance imaging measurements (Tang *et al.* 1999; Bathe & Kamm 1999; Buchanan Jr., Kleinstreuer & Comer 2000; Stroud, Berger & Saloner 2000).

The various stenotic flow experiments listed in § 1.2 confirmed the presence of highly disturbed flow downstream of a stenosis and even transition to turbulence in the presence of stenoses greater than 75 %. However, simulating turbulent flows in complex geometries involves overcoming several numerical obstacles, such as sufficient mesh resolution required to simulate all the scales of turbulence. At the same Reynolds number, it can be even more difficult to simulate transition to turbulence as opposed to fully turbulent flow because of the presence of localized small-scale structures that are transported with minimum physical dissipation, requiring sufficient spatial resolution and accurate long-time integration (Fischer, Kruse & Loth 2002).

With the exception of the numerical studies by Mallinger & Drikakis (2002), Mittal, Simmons & Najjar (2003), and Sherwin & Blackburn (2005), most stenotic flow simulations have been conducted in the laminar regime, failing to address the issue of turbulence in the post-stenotic field. The unsteady RANS predictions of pulsatile stenotic flows performed by Varghese & Frankel (2003) highlight the inability of traditional turbulence models to accurately predict all the complex flow features reported by experimentalists downstream of a stenosis. More recently, Ryval, Straatman & Steinman (2004) were able to obtain much improved RANS predictions for the same flows using improved inlet boundary conditions, in the form of the Womersley solution for laminar pulsatile flow through rigid tubes (Womersley 1955). While simulating physiological flows using simple two-equation turbulence models has shown some promise, these models are yet to be validated against detailed measurements of transitional and turbulent post-stenotic flow that can only be carried out via DNS or LES.

Mallinger & Drikakis (2002) conducted high-order simulations of instabilities in pulsatile flow through a three-dimensional axisymmetric stenosis, revealing the existence of flow instabilities throughout the pulsatile cycle that are manifested by highly asymmetric flow and helical disturbances downstream of the stenosis. Mittal *et al.* (2003) performed LES of pulsatile flow through a planar channel with a one-sided semicircular constriction and also found evidence of transition to turbulence in the downstream section. In both these studies a small, white-noise, random perturbation was imposed on all components of the inflow velocity to break the flow symmetry. Most recently, Sherwin & Blackburn (2005) conducted stability analyses of steady and pulsatile axisymmetric stenotic flows. They found that steady flow undergoes a Coanda-type wall attachment and turbulent transition through a subcritical bifurcation, while pulsatile flows become unstable through a subcritical period-doubling bifurcation involving alternating tilting of vortex rings that are ejected from the throat with each pulse and rapidly break down through a self-induction mechanism. Localized transition, followed by relaminarization further downstream, was observed at the physiologically realistic Reynolds numbers employed in their study.

1.4. *The present study*

The goal of the present study is to thoroughly detail, through direct numerical simulations, the instantaneous and statistical flow features that occur downstream of a

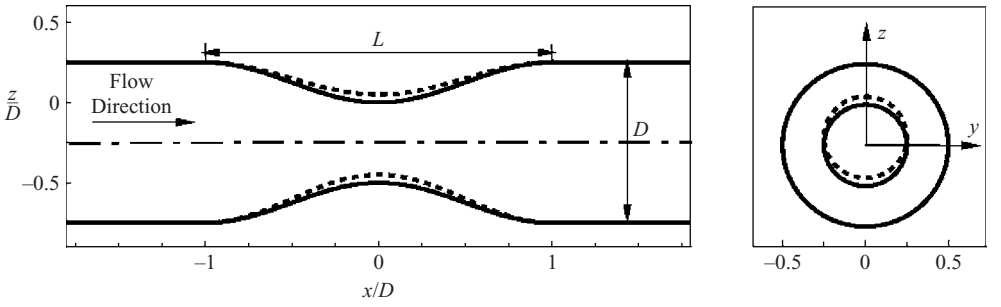

FIGURE 1. Side and front views of the stenosis geometry ($L = 2D$), the solid line corresponding to the profile of the axisymmetric model and the dashed line to the eccentric model; x is the streamwise direction while y and z are the cross-stream directions. The front view shows the cross-section corresponding to both models in the main vessel and at the throat, $x = 0$.

stenosis under both steady and pulsatile inflow conditions, complementing the information yielded by previous numerical studies. This idealized study has been conducted in terms of non-dimensional parameters to provide a fundamental basis for understanding the flow dynamics that may be generated by even more complex occlusions within the arterial tree. For the simulations, we used the spectral-element method, which allows geometric flexibility and non-conforming meshes for local refinement, while providing high-order accuracy. To maintain the physiologic relevance of the study and allow qualitative comparability, we stayed as close as possible to the classical stenotic flow experiments of Ahmed & Giddens (1983*a*, 1984). As in the experiments, wall compliance and non-Newtonian effects have been ignored. The focus of this work is to study post-stenotic transition to turbulence in the presence of a stenosis asymmetry, in contrast to the axisymmetric experimental model. To this end, a geometric perturbation in the form of an eccentricity was introduced at the stenosis throat. This resulted in asymmetries and disturbed flow in the post-stenotic region that were not observed in flow simulations using the axisymmetric model. The eccentric case is extremely relevant from the physiological standpoint because actual arterial stenoses are highly unlikely to exhibit any axisymmetry (Stroud *et al.* 2000).

The results obtained under steady inflow conditions are presented in this paper, while the pulsatile flow details are covered in Part 2 (Varghese, Frankel & Fischer 2007). The flow model and numerical method are detailed in § 2. Results and discussion, including comparison with experiments for the steady inflow case, are presented in § 3. Conclusions follow in § 4.

2. Problem formulation

Steady flow through both axisymmetric and eccentric stenotic flow models were studied, with both stenosis geometries corresponding to a maximum area restriction of 75 % at the throat. The baseline stenosis geometry modelled for this study was similar to that used in the stenotic flow experiments of Ahmed & Giddens (1983*a*, 1984) and is described in § 2.1. The numerical methodology employed for all the simulations reported here is outlined in § 2.2.

2.1. *Flow model and dimensionless groups*

Profiles of the axisymmetric and eccentric stenosis models are shown in figure 1. A cosine function dependent on the axial coordinate, x, was used to generate the

geometry shown. The cross-stream coordinates, y and z, were computed by using $S(x)$, specifying the shape of the stenosis as

$$\left.\begin{aligned} &S(x) = \tfrac{1}{2}D[1 - s_o(1 + \cos(2\pi(x - x_o)/L))], \\ &y = S(x)\cos\theta, \qquad z = S(x)\sin\theta, \end{aligned}\right\} \tag{2.1}$$

where D is the diameter of the non-stenosed tube, $s_o = 0.25$ for the 75 % area reduction stenosis used throughout this study, L is the length of the stenosis ($=2D$ in this study), and x_o is the location of the centre of the stenosis ($x_o - \frac{1}{2}L \leqslant x \leqslant x_o + \frac{1}{2}L$).

For the eccentric model, the stenosis axis was offset from the main vessel axis by $0.05D$. The offset, $E(x)$, and subsequently the modified y and z coordinates were computed as

$$\left.\begin{aligned} &E(x) = \tfrac{1}{10}s_o(1 + \cos(2\pi(x - x_o)/L)), \\ &y = S(x)\cos\theta, \qquad z = E(x) + S(x)\sin\theta. \end{aligned}\right\} \tag{2.2}$$

As equation (2.2) shows, the offset was introduced in the (x, z)-plane corresponding to $y = 0$ only. In both models, the upstream and downstream sections of the vessel extended for 3 and 24 vessel diameters, respectively, as measured from the stenosis throat (located at $x = 0$ in the figure).

For the steady flow simulations, the parabolic velocity profile for laminar fully developed Poiseuille flow was imposed at the inlet as

$$\frac{u}{u_i} = 2(1 - r^2), \qquad \frac{v}{u_i} = 0, \qquad \frac{w}{u_i} = 0, \tag{2.3}$$

where u, v and w are velocity components in the x-, y- and z-directions, respectively; u_i is the cross-sectional-averaged inlet velocity and $r = \sqrt{y^2 + z^2}$ is the radial distance from the vessel centreline.

The vessel walls were assumed to be rigid for all simulations within this study, with the no-slip boundary condition applied at the walls. All parameters and normalizations used here were chosen to match the flow conditions in the experiments by Ahmed & Giddens (1983*a*) to facilitate comparisons with their measurements. The simulations through the axisymmetric and eccentric stenosis models were both performed at Reynolds numbers of 500 and 1000, based on the vessel diameter D and mean inlet velocity u_i. All Reynolds numbers subsequently referred to in this paper have this definition.

2.2. *Numerical methodology*

The numerical simulations employed a spectral-element code, developed at Argonne National Laboratory, that is especially suited to simulation of transitional and turbulent flows in complex geometries, and is described by Fischer *et al.* (2002). The code is based on the non-conforming spectral-element method (SEM) for solution of the incompressible Navier–Stokes equations in $\Re^d$ (here, $d = 3$),

$$\left.\begin{aligned} &\frac{\partial \boldsymbol{u}}{\partial t} + \boldsymbol{u}\cdot\nabla\boldsymbol{u} = -\nabla p + \frac{1}{Re}\nabla^2\boldsymbol{u} \quad \text{in} \quad \Omega, \\ &\nabla\cdot\boldsymbol{u} = 0 \quad \text{in} \quad \Omega, \end{aligned}\right\} \tag{2.4}$$

where $\boldsymbol{u} = (u, v, w)$ is the velocity vector, p is the pressure, and $Re = UL/\nu$ is the Reynolds number based on a characteristic velocity, length scale, and kinematic

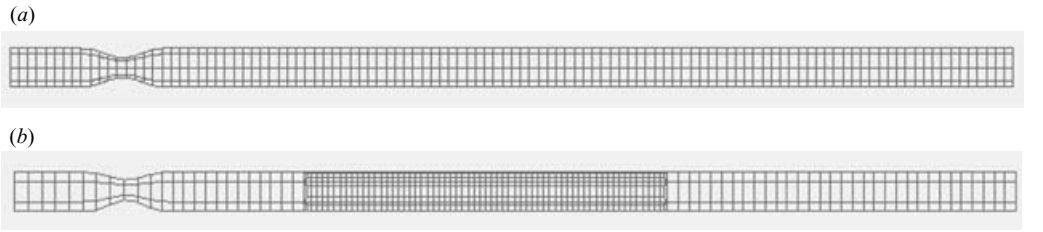

FIGURE 2. Layout of spectral element mesh. (*a*) Axisymmetric stenosis model with $K = 2240$ hexahedral cells, and (*b*) eccentric stenosis model with $K = 2448$ hexahedral cells.

viscosity. The associated initial and boundary conditions are

$$\left.\begin{aligned} &\boldsymbol{u}(\boldsymbol{x}, 0) = \boldsymbol{u}^0(\boldsymbol{x}), \\ &\boldsymbol{u} = \boldsymbol{u}_v \quad \text{on} \quad \partial\Omega_v, \\ &\nabla u_i \cdot \hat{\boldsymbol{n}} = 0 \quad \text{on} \quad \partial\Omega_o, \end{aligned}\right\} \tag{2.5}$$

where $\hat{\boldsymbol{n}}$ is the outward pointing normal on the boundary and subscripts v and o indicate boundary regions where Dirichlet velocity or Neumann outflow boundary conditions are specified, respectively.

Temporal discretization of the Navier–Stokes equations (2.4) was based on the high-order operator-splitting methods developed by Maday, Patera & Rønquist (1990). This approach separates the linear viscous term from the nonlinear advection contribution. Time integration of the advection term was advanced quickly by using an explicit scheme, while the linear symmetric Stokes problem was solved implicitly. Third-order-accurate time-stepping was employed for all the simulations, except in the case of pulsatile flow through the eccentric stenosis, for which time-stepping was of the second order, owing to its better stability properties (Deville, Fischer & Mund 2002). The solution was further stabilized by using the filter developed by Fischer & Mullen (2001).

The spatial discretization was based on the $P_N - P_{N-2}$ spectral-element method, which represents velocity (N) and pressure ($N - 2$) as Nth-order tensor product Lagrange polynomials, based on Gauss or Gauss–Lobatto (GL) quadrature points, within each of K computational mesh cells. The total number of grid points is approximately KN^3. SEM couples the efficiency of global spectral methods with the geometric flexibility of finite elements provided by non-conforming deformed hexahedral elements. A representative mesh employed for the axisymmetric model simulations and comprising $K = 2240$ hexahedral cells is shown in figure 2(*a*). The method provided accurate solutions with minimal numerical dissipation and dispersion. Further details on the discretization and solution procedure, along with temporal and spatial convergence results, can be found in the literature (Fischer 1997; Deville *et al.* 2002).

2.2.1. *Outflow boundary condition treatment*

In turbulent flows, it is possible to have vortices strong enough to yield a (locally) negative flux at the outflow boundary. Since no flow characteristics are specified on these boundaries, a negative flux condition typically leads to instabilities with catastrophic results. One way to ensure that the characteristics at the exit are always pointing outwards is to force the exit flow through a nozzle, effectively adding a mean axial component to the velocity field. In contrast, schemes based on viscous

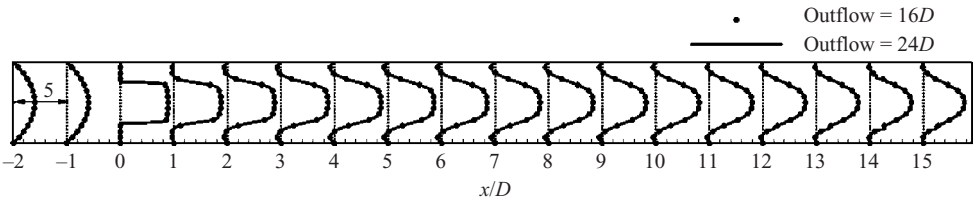

FIGURE 3. Comparison of axial velocity profiles, u/u_i, for steady flow through the 75% axisymmetric stenosis model at $Re = 1000$ for two outflow lengths, $16D$ and $24D$ (as measured from the stenosis throat). The profiles are offset from each other axially and the scale is indicated. A similar format is employed to present profiles in subsequent figures.

buffer zones require knowledge of the anticipated space and time scales to ensure that vortical structures are adequately damped as they pass through the buffer zone.

This nozzle effect can be imposed numerically without having to change the mesh geometry by imparting a positive divergence to the flow field near the exit (in the spirit of a supersonic nozzle). In the current study, this is done by identifying the layer of elements adjacent to the outflow and imposing a divergence function $D(x)$ that is zero at the upstream end of the layer and ramps to a fixed positive value at the exit. Specifically, we set $D(x) = C[1 - (x_\perp/L_\perp)^2]$, where $x_\perp$ is the distance normal to the boundary and $L_\perp$ is the maximum thickness of the last layer of elements. A net gain in mean velocity is obtained over the extent of the layer by integrating the expression for D from $x_\perp/L_\perp = 1$ to 0. The constant C is chosen such that the gain is equal to the mean velocity prior to the correction.

The results of this fix are illustrated in figure 3 by comparing axial velocity profiles for steady flow through the 75% axisymmetric stenosis at $Re = 1000$, obtained using outflow vessel lengths of $16D$ and $24D$ (as measured from the stenosis throat). The profiles show that there is no difference between the two cases, even close to the outflow region, $x > 14D$, indicating that the outflow treatment does not pollute the solution far upstream of the boundary. This was observed to be the case for all the simulations performed for this study, both axisymmetric and eccentric models. The results presented in the following sections were all obtained on computational domains with outflow lengths of $24D$.

2.3. *Data reduction*

We define here the averaging operations employed in this study. Under conditions of steady inlet flow, for a generic flow variable f, the time-averaged mean over a period of time T_f is computed as

$$\overline{f}(x, y, z) = \frac{1}{T_f} \int_{t_0}^{t_0+T_f} f(x, y, z, t)\, \mathrm{d}t, \tag{2.6}$$

where t_0 is the time at which the averaging process is initiated. The deviation from this average, which represents the random turbulent fluctuations, is then defined as

$$f'(x, y, z, t) = f(x, y, z, t) - \overline{f}(x, y, z). \tag{2.7}$$

Root mean square (r.m.s.) quantities are subsequently computed as

$$f'_{rms} = \sqrt{\overline{f'^2}}. \tag{2.8}$$

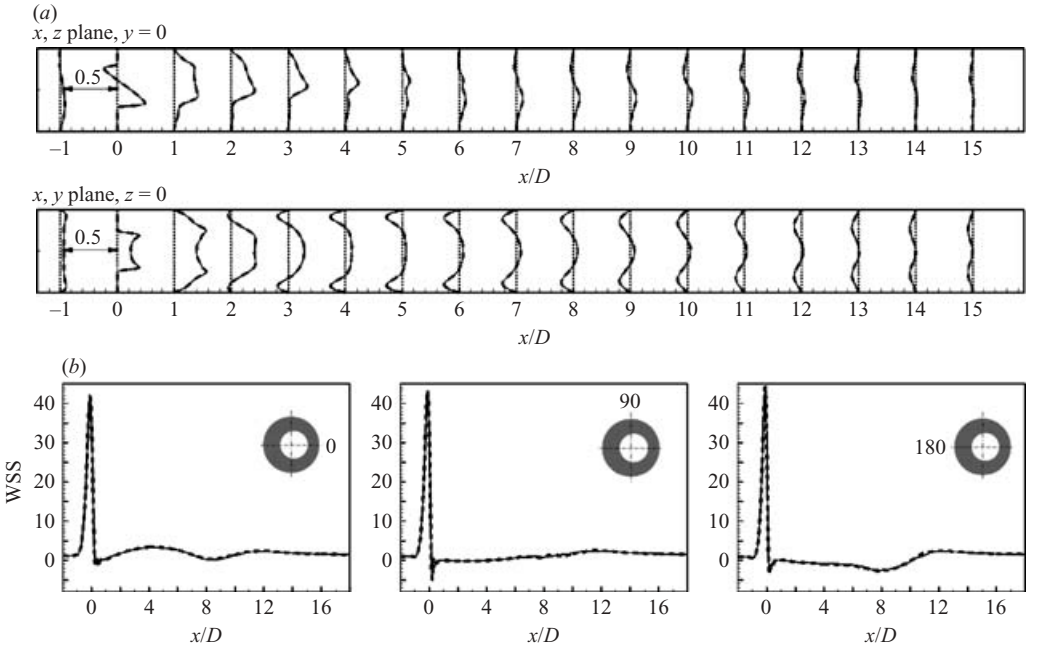

FIGURE 4. Resolution studies for steady flow through the 75 % eccentric stenosis model. Results were obtained on two meshes, corresponding to $K = 2240$, $N = 8$ (dashed line) and $K = 2240$, $N = 11$ (solid line). (a) Cross-stream velocity profiles, w/u_i, for $Re = 500$. (b) Axial wall shear stress (WSS) for $Re = 1000$. The circumferential locations at which WSS was obtained are indicated.

2.4. *Grid resolution and simulation details*

Numerical convergence studies performed for the case of steady flow through the axisymmetric stenosis confirmed that the spatial resolution was sufficient. Simulations were performed on two sets of grids, both with $K = 2240$ hexahedral cells, the outline of which is shown in figure 2(a). Axial and cross-stream velocity profiles (not shown) obtained with polynomial orders $N = 8$ and $N = 11$, effectively increasing the number of grid points from approximately 1.15 million to almost 3 million, were found to match exactly.

The outline of the mesh used for the eccentric model calculations is shown in figure 2(b). As the figure shows, the number of hexahedral cells in the region $4D \leqslant x \leqslant 14D$, where turbulent breakdown was expected, was increased by a factor of eight. Figure 4(a) compares cross-stream velocity profiles obtained for steady flow through the eccentric model at $Re = 500$ using two different polynomial orders of $N = 8$ and $N = 11$, on the same spectral element mesh. The profiles obtained with the two computational meshes can be seen to agree very well. Similar meshes used for the $Re = 1000$ case, when post-stenotic flow transitioned to turbulence, showed that the resolution was satisfactory. Figure 4(b) compares axial wall shear stress at three circumferential locations for the turbulent case. Similar results obtained on a mesh with a polynomial order of $N = 13$ matched exactly those obtained using the lower resolution meshes and further confirmed that grid independence had been achieved.

In the case of the axisymmetric stenosis model, initial conditions for the steady flow simulations were set by starting the computations with typically large viscosity ($Re \approx 10$). The viscosity was subsequently lowered after a few thousand time-steps

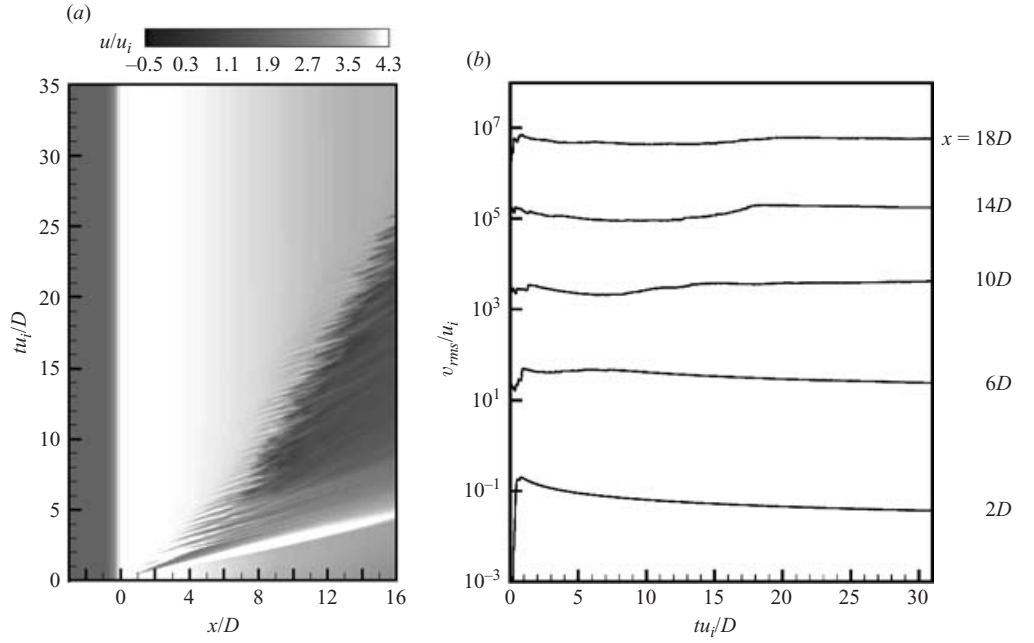

FIGURE 5. (*a*) Contours of centreline axial velocity, u/u_i, from the start of the simulation till steady state was reached, for steady flow flow through the 75 % axisymmetric stenosis at $Re = 1000$. (*b*) Log plot of cross-stream r.m.s. velocity, v_{rms}/u_i, versus time at five axial stations along the vessel centreline, for steady flow through the eccentric stenosis at $Re = 1000$. The r.m.s. velocity at each axial station is offset by 100 log units.

while simultaneously increasing the inlet velocity to ultimately match the Reynolds numbers considered here, $Re = 500$ and 1000. Steady-state (time-invariant) results from these simulations were employed as initial conditions for the corresponding eccentric model computations. The results presented in the following sections were obtained after confirming that initial transients had left the computational domain. For both stenosis models, the velocity at 75 axial locations along the vessel were monitored to ensure that a steady state (or statistically steady state for the turbulent case) had been achieved. Figure 5(*a*) shows the variation of axial velocity along the centreline of the vessel during the first 35 non-dimensional time units of simulation for the axisymmetric case at $Re = 1000$. Root-mean-square velocities were also continuously monitored and results were obtained only after these were deemed to have statistically converged. Figure 5(*b*) shows a log plot of cross-stream r.m.s. velocity, v_{rms}/u_i, at five axial stations along the centreline during the first 30 non-dimensional time units after the simulation of flow through the eccentric model at $Re = 1000$ was initialized. For this case, turbulent statistics presented in § 3.2.2 were collected only after $tu_i/D = 25$.

Non-dimensional time-step sizes of 1.0×10^{-3} and 2.5×10^{-4} were used for the axisymmetric and eccentric cases, respectively (on the highest resolution meshes). Axisymmetric model simulations on the $K = 2240$, $N = 11$ mesh took less than one wall-clock day to reach steady-state on 256 processors of the IBM BGL machine at Argonne National Laboratory. The most computationally demanding eccentric model simulation, on the $K = 2448$, $N = 13$ mesh, was run on up to 1024 processors of the

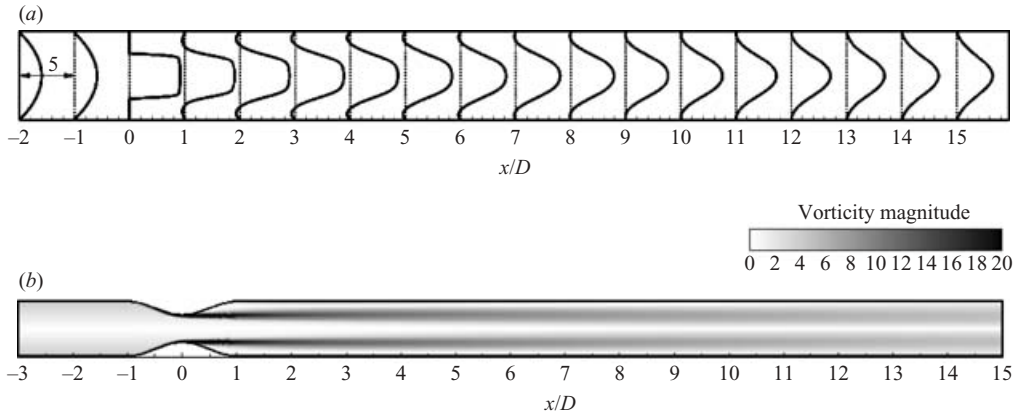

FIGURE 6. (*a*) Axial velocity profiles, u/u_i, and (*b*) vorticity magnitude, normalized by u_i/D, for steady flow through the 75 % axisymmetric stenosis at $Re = 500$. Similar normalizations are employed in all subsequent presentations of steady flow results.

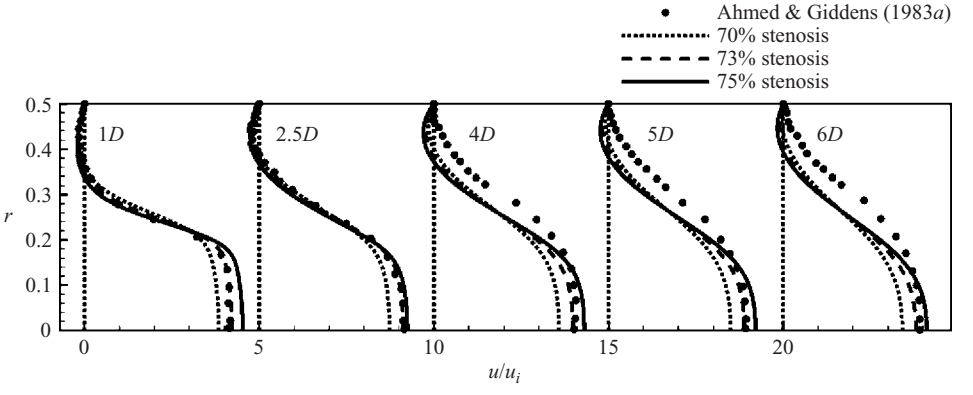

FIGURE 7. Comparison of axial velocity profiles at downstream locations with experimental profiles for steady flow through the axisymmetric stenosis at $Re = 500$. The axial stations are indicated in terms of diameters downstream from the stenosis throat.

same machine. Computing time for this simulation was close to 22 wall-clock hours for 160 000 time-steps (corresponding to $tu_i/D = 20$).

3. Results and discussion

3.1. *Axisymmetric model*

Axial velocity profiles and vorticity magnitude contours in figure 6 show a laminar axisymmetric jet and shear layer for the 75 % axisymmetric stenosis with an inlet Reynolds number of 500. The fluid accelerates through the constriction creating a plug-like velocity profile within the stenosis and a flow separation region immediately downstream. The peak velocities in the immediate downstream section exceed the mean inlet velocity (u_i) by more than a factor of four. Axial velocity profiles at five axial stations downstream of the stenosis are compared with digitized experimental results of Ahmed & Giddens (1983*a*) in figure 7. In order to highlight the sensitivity of

flow physics to the stenosis degree, profiles computed for models with area reductions of 70 % and 73 % are also shown, the stenosis length being kept constant at $2D$ throughout. The profiles predicted for the 73 % model match exactly with the experiments immediately downstream of the stenosis, at locations $x = 1D$ and $2.5D$. Further downstream the profiles diverge, especially close to the wall, where absolute differences between the numerics and experiments are as large as 20 %. The experimental profiles in this region are considerably fuller than their computed counterparts, with the size of the separation zone reducing with axial distance and flow completely reattaching to the wall between $x = 4D$ and $6D$, suggesting that the flow is not completely laminar. In the current simulation, however, separation continues well beyond this location, with the flow downstream of the 75 % stenosis reattaching at $x \approx 11D$, as shown in figure 6(a). The flow maintains its jet-like character as far downstream as $x = 15D$, with peak velocity at this location attaining values more than three times the mean, 50 % larger than the $2u_i$ peak velocity for the inlet Poiseuille solution.

The downstream flow field predicted here is laminar and axisymmetric with no evidence of jet breakdown and shear layer oscillation. A very similar flow field is predicted for the $Re = 1000$ case, as can be seen in the velocity profiles in figure 3. At the higher Reynolds number, the flow does not reattach even as far as $x = 15D$. Vorticity magnitude contours are qualitatively similar to those in figure 6(b).

3.2. *Eccentric model*

At an inlet Reynolds number of 500, the velocity and vorticity results in figures 8 and 9, respectively, illustrate the effect of a $0.05D$ eccentricity at the stenosis throat. Axial velocity levels above zero have been blanked out in figure 8(b) to highlight reverse flow regions. While the streamwise velocity in the stenosis exhibits the same plug-shaped profile as in the axisymmetric model, with peak velocity greater than $4u_i$, the in-plane velocity vectors show that strong crossflow velocities, created by the geometric perturbation, deflect the jet toward the side of the eccentricity. The biasing of the stenotic jet is clearly highlighted by the velocity profiles and vorticity magnitude contours in the plane of eccentricity (corresponding to $y = 0$). The accelerating jet causes flow separation along the side of the vessel that is farther away from the stenosis, forming a rather large recirculation region that covers almost half the vessel section at $x = 2D$, as indicated by the dark-shaded region in figure 8(b). Further downstream, the crossflow velocity vectors are deflected along the walls and form a pair of weak counter-rotating vortices along the edge of the recirculation region. These entrain more fluid from the jet into the recirculation zone, causing it to recede along the walls, while extending farther into the vessel core. Flow separation extends as far as the centreline in the region between $x = 6D$ and $8D$. At this point, the jet is deflected by the wall back toward the vessel centre, causing the recirculation zones to recede. Complete flow reattachment occurs only after $x \approx 14D$.

Figure 8(a) shows that the movement of the jet and the recirculation region is symmetric about the $z = 0$ plane, which bisects the tube perpendicular to the plane of eccentricity. Note that the stenosis is also symmetric about this plane. The initial biasing of the jet away from the $z = 0$ plane is clear, resulting in lower velocities along the vessel centreline as the recirculation zone creeps up toward the core. With the jet being directed back to the centre after $x = 8D$ and centreline velocities once again starting to increase, the profiles begin to acquire a more uniform shape in this plane, as seen at $x = 21D$ and $22D$. However, in the $y = 0$ plane, the flow continues to maintain its jet-like character in the far downstream region, as shown in the velocity profile and vorticity plots. The profiles in this plane tend more toward those predicted

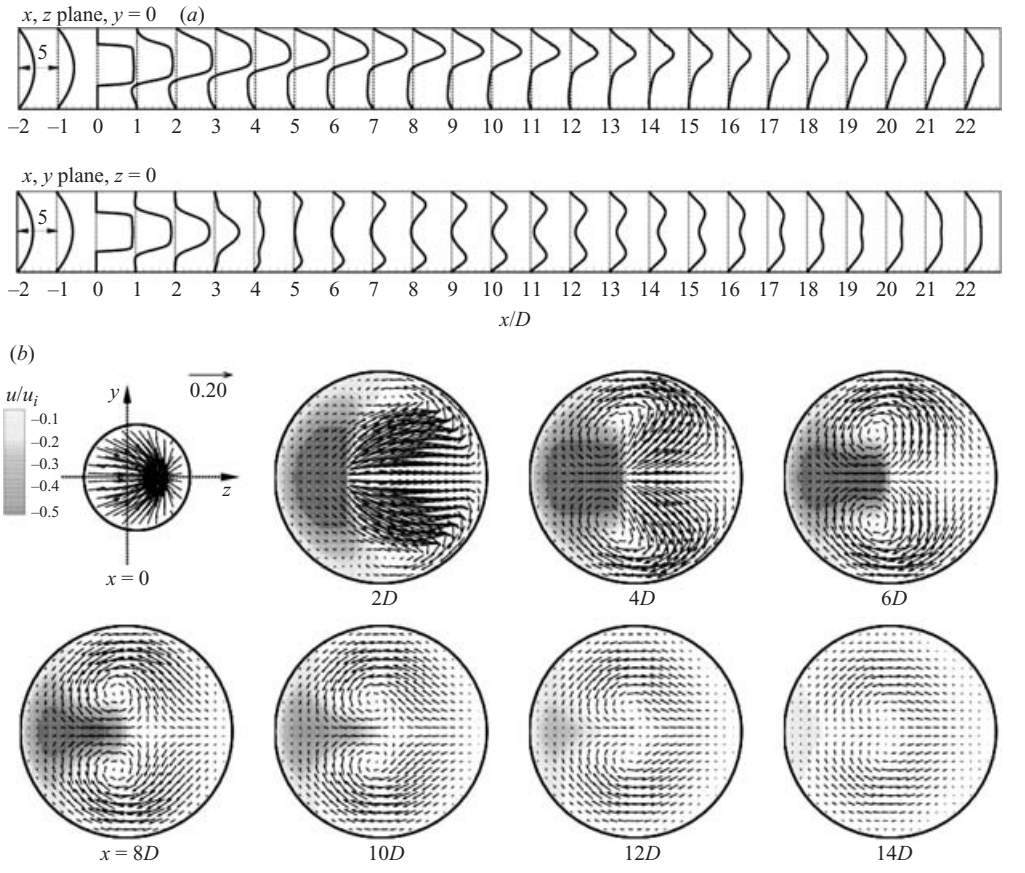

FIGURE 8. Steady flow through the 75 % eccentric stenosis at $Re = 500$. (*a*) Axial velocity profiles, and (*b*) in-plane velocity vectors superimposed on axial velocity contours at downstream stations (the dark regions indicate negative velocity, i.e. into the page).

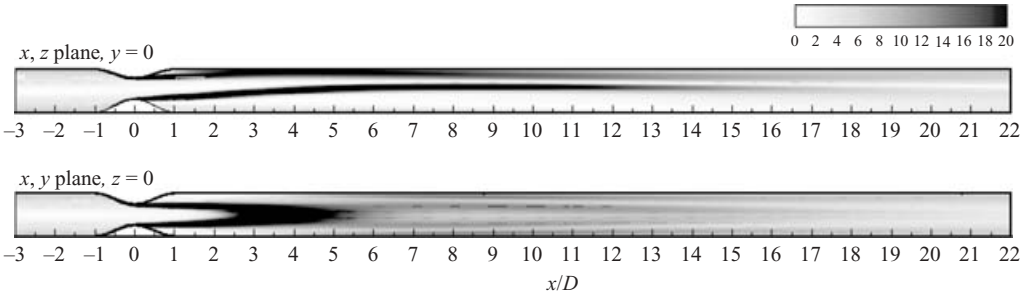

FIGURE 9. Vorticity magnitude contours for steady flow through the 75 % eccentric stenosis at $Re = 500$.

for the axisymmetric model, with peak velocities of about $3u_i$ at $x = 14D$. The results suggest that the flow will eventually resemble a weak elliptic jet far downstream of the stenosis throat, with its major axis aligned with the $z = 0$ plane, before reverting to the parabolic inlet profile. At this Reynolds number, however, the flow is essentially laminar across the entire post-stenotic region, with no evidence of flow disturbances.

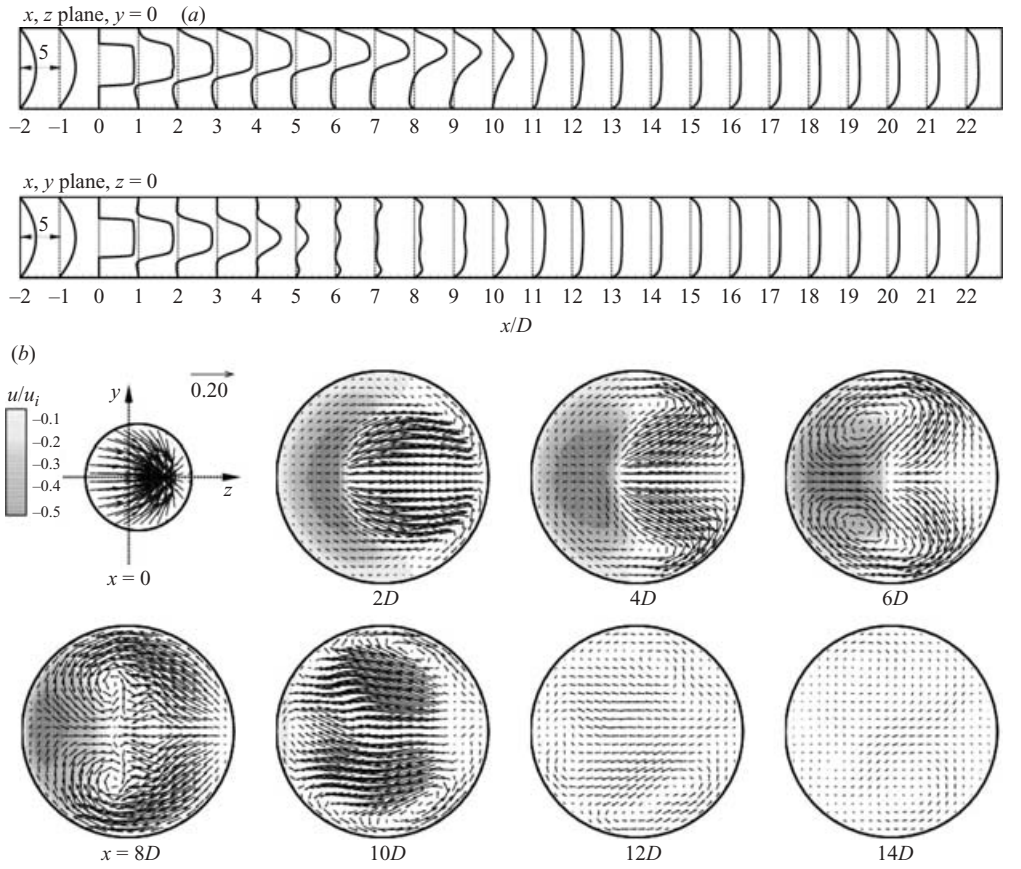

FIGURE 10. Time-averaged results for steady flow through the 75% eccentric stenosis at $Re = 1000$. (*a*) Axial velocity profiles, and (*b*) in-plane velocity vectors superimposed on axial velocity contours at downstream stations (the dark regions indicate negative velocity, i.e. into the page).

3.2.1. *Transition to turbulence: evolution of averaged flow characteristics*

Unlike the axisymmetric cases, when the inlet Reynolds number is increased to 1000 for the eccentric model, the flow characteristics in the post-stenotic region alter considerably, with localized transition occurring after approximately $x = 4D$. The time-averaging operation defined in equation (2.6) was employed for this case over a non-dimensional time $T_f u_i/D = 200$ and the time-averaged results are presented in figures 10 and 11.

Velocity profiles in both the vessel bisecting planes and in-plane vectors closely match those seen at $Re = 500$ until about $x = 3D$. The stenotic jet is deflected toward the wall along the side of the eccentricity, creating a distinct crescent-shaped recirculation zone along the opposite side. As at the lower Reynolds number, the crossflow velocities at $x = 2D$ are deflected by the wall and reduce the extent of the recirculation region along the walls, at the same time pushing it up to the centreline. Farther downstream, the differences between this simulation and its low-Reynolds-number counterpart become readily apparent upon comparing the corresponding recirculation zones, namely the dark-shaded regions of figures 8(*b*) and 10(*b*), in which positive axial flow regions have been blanked out.

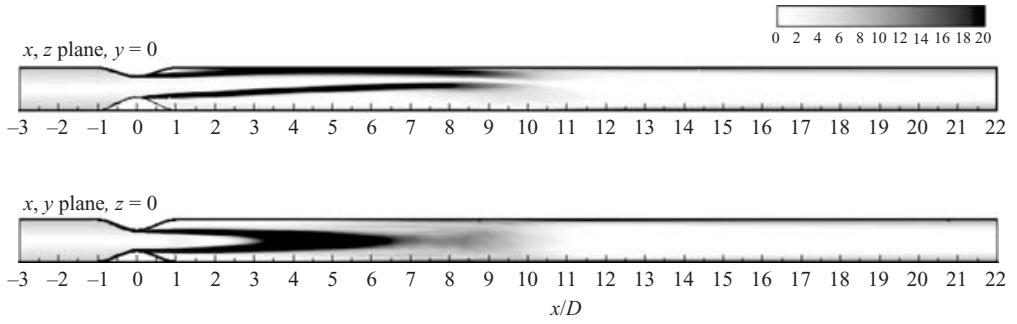

FIGURE 11. Time-averaged vorticity magnitude contours for steady flow through the 75 % eccentric stenosis at $Re = 1000$.

At $Re = 1000$, almost half the cross-section experiences negative velocities in the vicinity of the $x = 4D$ station. The stenotic jet starts to break down after $x = 6D$, as the jet is deflected back toward the centre. The relatively large crossflow velocities in this region (as compared with those between $x = 6D$ and $10D$ at $Re = 500$) push the recirculation region back along the walls until it recedes completely within the length of a few vessel diameters. As evidenced by the velocity profiles in figure 10(a), the flow fully reattaches by $x \approx 10D$, almost four vessel diameters earlier than the low-Reynolds-number case. Vorticity magnitude contours in figure 11 confirm complete breakdown of the jet and shear layer by $x = 11D$.

In the far downstream section, $x \geqslant 12D$, the velocity differential across the vessel section disappears, and axial velocity profiles take on a uniform shape that is more typical in turbulent flows, with peak velocities close to $1.5u_i$. Beyond $x = 13D$, the profiles start to regress toward their normal laminar (parabolic) shape with centreline velocity increasing and near-wall velocities decreasing. However, profiles at $x = 21D$ and $22D$ indicate that the flow has not completely relaminarized even at this distance, with centreline velocities approximately $1.5u_i$, lower than the $2u_i$ peak velocity for the inlet Poiseuille solution.

3.2.2. *Turbulent statistics*

The intensity of any turbulent flow can be gauged by studying the r.m.s. velocities, $\sqrt{\overline{u'^2}}$, $\sqrt{\overline{v'^2}}$, and $\sqrt{\overline{w'^2}}$, defined in § 2.3. The three normal Reynolds stress components, $\overline{u'^2}$, $\overline{v'^2}$, and $\overline{w'^2}$ are a measure of the kinetic energy per unit mass of the velocity fluctuations in each of the coordinate directions, and the turbulent kinetic energy, or the kinetic energy of the turbulent fluctuations per unit mass, can in turn be defined as $k = \frac{1}{2}\overline{u_i' u_i'}$ (Tennekes & Lumley 1972; Wilcox 1993).

Streamwise and cross-stream r.m.s. velocity profiles are shown in figure 12, with mean inlet velocity u_i used for non-dimensionalization. In both planes the streamwise r.m.s. velocity u_{rms}/u_i is amplified considerably on moving farther away from the stenosis throat, especially after $x = 4D$ where peak values, $(u_{rms})_{max}$, are almost 40 % of u_i. At axial stations preceding $x = 7D$, peak r.m.s. levels occur along the shear layer. However, as the shear layer breaks up in the region $x > 6D$ the turbulent energy is redistributed across the entire cross-section of the vessel. This is also clear from the distribution of turbulent kinetic energy profiles in the post-stenotic region, shown in figure 13. These profiles are non-dimensionalized by u_i^2 and qualitatively match the streamwise r.m.s. velocity profiles at each axial location. The peaks in the profiles immediately downstream of the stenosis show that turbulent energy is concentrated

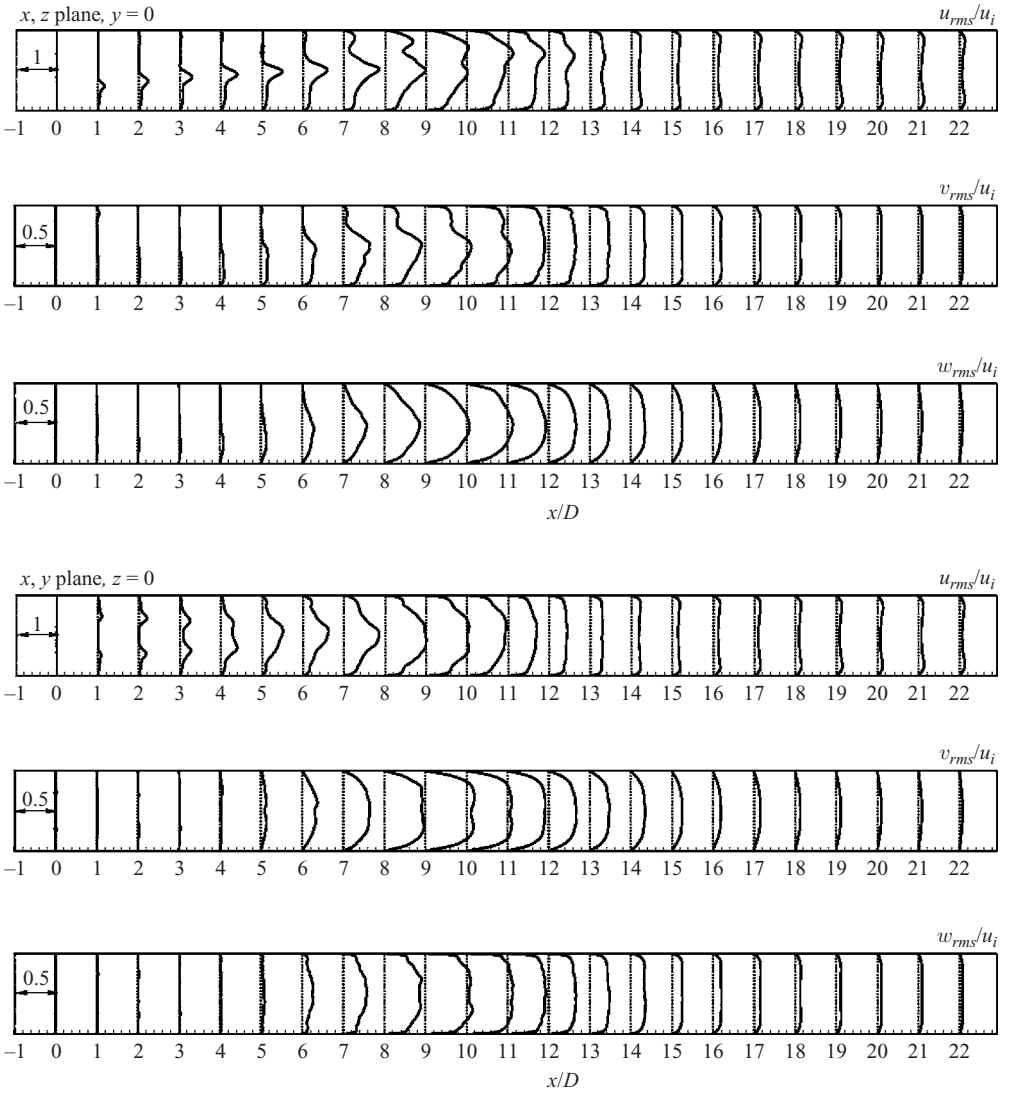

FIGURE 12. Root-mean-square velocity profiles, normalized by mean inlet velocity u_i, for steady flow through the 75 % eccentric stenosis at $Re = 1000$.

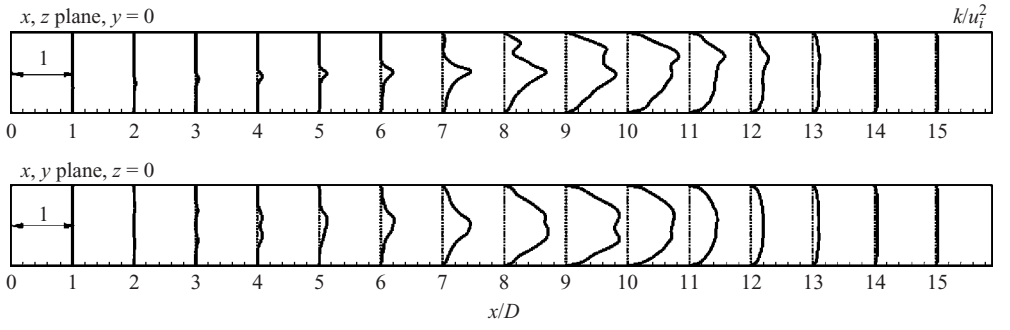

FIGURE 13. Turbulent kinetic energy (k) profiles, normalized by u_i^2, for steady flow through the 75 % eccentric stenosis at $Re = 1000$.

in the shear layer, indicating that the instability initially propagates along the shear layer. Only after $x \approx 7D$ do the profiles tend to a more uniform nature, as a result of turbulent jet breakdown and disturbances rapidly diffusing over the cross-section, smearing the peaks with increasing axial distance. Turbulent kinetic energy and u_{rms} attain maximum levels in the turbulent region between $x = 7D$ and $x = 11D$, with $(u_{rms})_{max} \approx 1.1u_i$ at $x = 10D$. After the flow has completely reattached at $x \approx 10D$, streamwise r.m.s. velocity profiles acquire a more uniform shape, but levels drop from more than $0.9u_i$ at $x = 11D$ to less than $0.2u_i$ at $x = 15D$ as viscous effects dominate and the flow relaminarizes. Correspondingly, the turbulent energy attenuates after $x = 11D$, eventually decaying to almost negligible levels close to the outflow.

Profiles of v_{rms} and w_{rms} in figure 12 show that the cross-stream turbulent velocities follow the trend of the streamwise turbulent velocity profiles, with sharp amplification occurring after $x = 5D$. Peak values in this region are approximately $0.1u_i$ and increase to about $0.2u_i$ as the shear layer starts to break up at around $x \approx 6D$. The subsequent breakdown region experiences the highest levels of turbulent energy generated by these cross-stream velocity fluctuations, with peak values rising to almost $0.6u_i$ between $x = 9D$ and $10D$. Further downstream, as seen in the streamwise r.m.s. data, v_{rms} and w_{rms} tend to become more evenly distributed across the vessel section while their magnitude continues to drop, eventually falling to approximately $0.1u_i$ at $x = 15D$. Comparing the streamwise and cross-stream turbulent velocities, one sees that immediately downstream of the stenosis most of the turbulent kinetic energy is siphoned off to the streamwise fluctuations before being redistributed to the other components by $x = 11D$, with u_{rms} almost always 50 % larger than both v_{rms} and w_{rms} across the entire turbulent section. This also indicates that turbulent breakdown is non-isotropic, an observation made by Deshpande & Giddens (1980) in their study of steady flow through a 75 % axisymmetric stenosis (similar to the one used in this study), albeit at a much higher Reynolds number of 15 000.

3.2.3. *Energy spectra*

Since transitional and turbulent flows contain a continuous spectrum of scales (i.e. with a wide separation of eddy sizes) it is usually worthwhile to characterize the nature of flow instabilities in terms of the frequency or spectral distribution of energy. The energy spectrum of the velocity signal is a measure of the frequency distribution of the energy contained within the turbulent fluctuations. To enable comparisons with previous experimental work (Cassanova & Giddens 1978; Deshpande & Giddens 1980; Ahmed & Giddens 1983*b*; Lu *et al.* 1983), we have defined the normalized spectrum, E^*, and Strouhal number, N_s, as

$$E^* = \frac{E(f)u_j}{2\pi d}, \qquad N_s = \frac{2\pi f d}{u_j}, \tag{3.1}$$

respectively. $E(f)$ is the frequency spectrum of the normalized streamwise velocity fluctuations $(u'/u_{rms})^2$, while f is the frequency of the fluctuation. As discussed by the above-cited experimentalists, the mechanisms governing the formation of instabilities and transition to turbulence in the post-stenotic region are dominated by the characteristics of the constriction rather than the main vessel. To reflect this, we have used the mean velocity at the stenosis throat $u_j(=4u_i)$ and minimum stenosis diameter $d(=0.5D)$ as the characteristic velocity and length scale used to normalize the energy spectra in equation (3.1).

The frequency spectra $E(f)$ were computed by using Welch's overlapping averaged modified periodogram method (Welch 1967). The data were divided into four segments

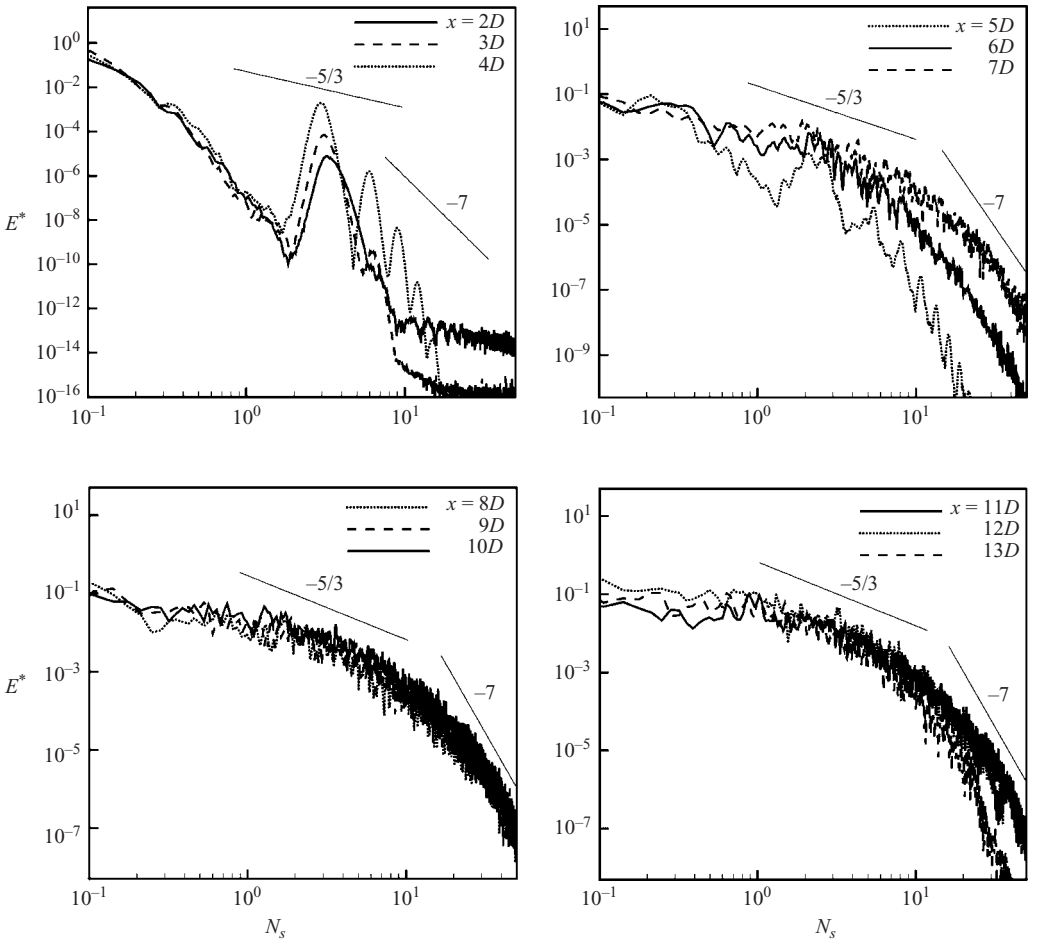

FIGURE 14. Normalized energy spectra of centreline streamwise velocity fluctuations, u' normalized by u_{rms} for steady flow through the 75 % eccentric stenosis at $Re = 1000$.

with 50 % overlap, each section windowed with a cosine taper window (Hann window) to reduce leakage, and four modified periodograms were computed and averaged. The data sampling rate was 2 kHz, corresponding to a Nyquist frequency of 1 kHz.

Figure 14 shows normalized centreline disturbance energy spectra at various axial stations downstream of the stenosis throat. Motivated by the spectral analysis work by Mittal *et al.* (2003), the lines corresponding to $N_s^{-5/3}$ and N_s^{-7} have also been included in the figure. In turbulent flows, the $-5/3$ slope is associated with the range of wavenumbers in which the energy cascade is dominated by inertial transfer, i.e. the inertial subrange, while the N_s^{-7} variation characterizes the dissipation range where viscous forces dominate (Tennekes & Lumley 1972; Hinze 1975; Wilcox 1993).

Between $x = 2D$ and $4D$, energy is concentrated within a narrow frequency band, resulting in a peak at approximately $N_s = 3.14$. This indicates the passage of vortices through these locations at a relatively low vortex shedding frequency or Strouhal number (fd/u_j) of 0.5. The intensity of the spectral peak rises with increasing axial distance, indicating more energy transfer into the starting vortex structure. As suggested by a reviewer, multiple peaks seen at locations $x = 3D$ and $4D$ are probably

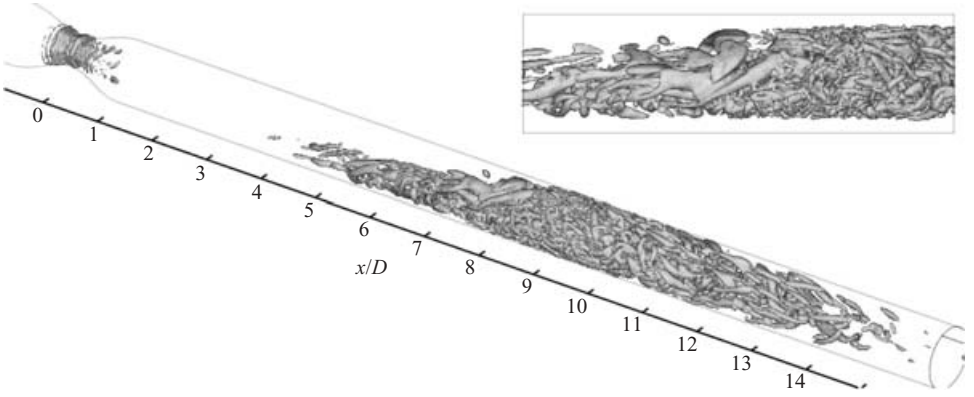

FIGURE 15. Instantaneous coherent structures (vortices) identified by using the isosurface corresponding to the negative contour −2.0 of the λ_2 criterion of Jeong & Hussain (1995), normalized by u_i/D, for steady flow through the 75 % eccentric stenosis at $Re = 1000$. The inset shows a close-up view of the structures in the region $6D \leqslant x \leqslant 10D$.

harmonics of the shedding frequency as the streamwise vortices become more powerful and increasingly nonlinear. The slight decrease in shedding frequency (with increasing axial distance from the stenosis) is another indication of this phenomenon. As these vortices are convected downstream, they start to break down into smaller structures, resulting in the peaks at $x = 5D$ being dispersed over a broader range of frequencies with a slope of $-5/3$, corresponding to the inertial subrange. Farther downstream, at $x = 6D$ and beyond, the peaks characterizing discrete-frequency phenomena are no longer present, and broadband spectra, characteristic of energy transfer between randomly distributed eddies in turbulent flows, are seen. At these locations, however, the range of frequencies comprising the inertial subrange is fairly short, indicating that the energy cascade from the largest to the smallest eddies in the post-stenotic region does not occur over a large frequency range as in fully developed turbulent flows. The region between $x = 6D$ and $10D$ is most turbulent, with intensities dropping after $x = 10D$, confirming the observations in § 3.2.2. The range of frequencies over which the inertial subrange extends before rolling off to the -7 range becomes shorter as viscous effects start to dominate in the region $x > 10D$.

3.2.4. *Turbulence structure*

Instantaneous coherent structures, shown in figure 15 and clearly identified by isosurfaces of a negative contour of the λ_2 criterion of Jeong & Hussain (1995), together with contours of streamwise velocity fluctuations in figure 16, give an appreciation of the nature of turbulent breakdown in the post-stenotic flow field. In the region between $x = 6D$ and $8D$, an array of streamwise vortices starts to form. These vortices extend over an axial length of approximately half the main vessel diameter and closely resemble the hairpin vortices observed by Klebanoff, Tidstrom & Sargent (1962) in their seminal investigations of laminar–turbulent transition in boundary layers. A hairpin vortex is a streamwise inclined Ω-shaped vortex that has a spanwise arch in the shape of a horseshoe. The instability that propagates along the shear layer in the form of a wave-like roll-up, similar to the Kelvin–Helmholtz instability associated with highly inflectional velocity profiles in typical shear flows, is clearly highlighted by contours of streamwise velocity fluctuations. In the region beyond $x = 8D$, the streamwise vortices, deemed to play an important role in pipe

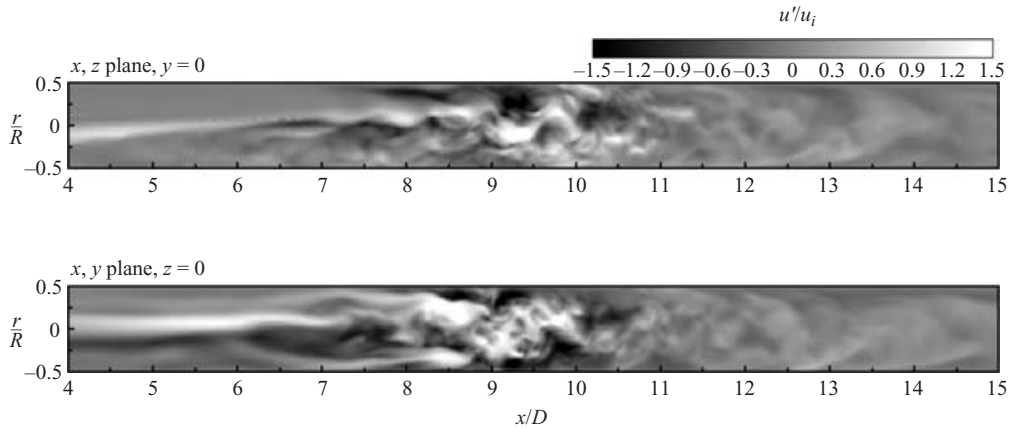

FIGURE 16. Instantaneous contours of streamwise velocity fluctuations u'/u_i, in the post-stenotic turbulent region for steady flow through the 75% eccentric stenosis at $Re = 1000$.

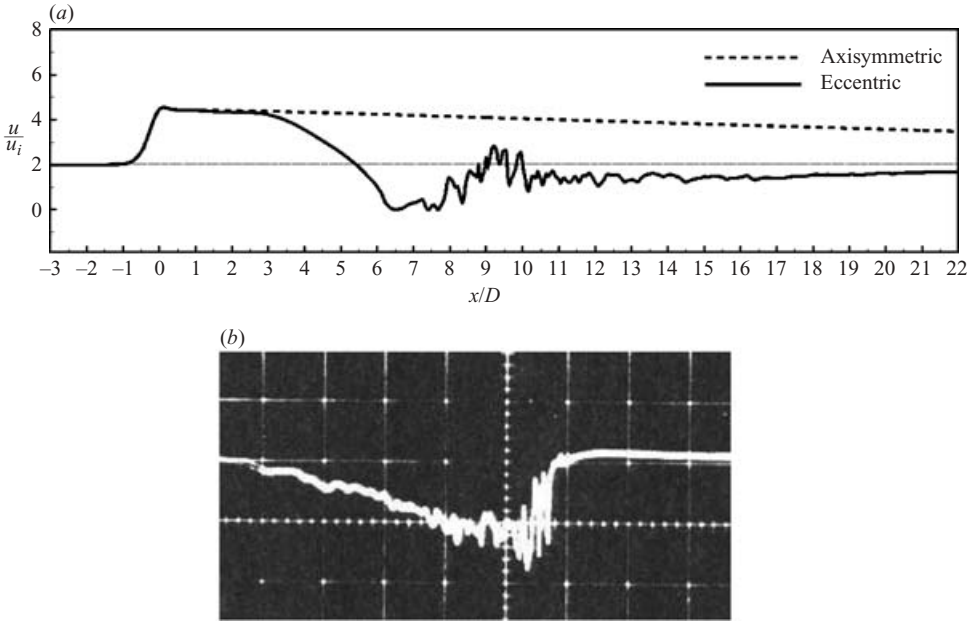

FIGURE 17. (*a*) Variation of instantaneous streamwise velocity u/u_i, along the centreline of the vessel for steady flow through the 75% axisymmetric and eccentric stenosis models at $Re = 1000$. (*b*) A time trace of streamwise velocity (along the centreline) associated with a turbulent puff, obtained for pipe flow at $Re = 2360$ (Wygnanski *et al.* 1975).

flow transition by previous investigators (Eliahou, Tumin & Wygnanski 1998; Shan *et al.* 1999; Han, Tumin & Wygnanski 2000) by rendering the flow unstable to three-dimensional disturbances, instigate abrupt turbulent breakdown. This gives rise to a turbulent spot that occupies the entire cross-section between $x \approx 9D$ and $11D$. The turbulent statistics and energy spectra presented in the previous sections indicate that turbulence intensity levels are highest within this spot.

Instantaneous streamwise velocity variations along the vessel axis are in effect the signatures left by the turbulent structures. In figure 17(*a*) they are presented along

with corresponding results for the laminar axisymmetric case at the same Reynolds number. The gradual deficit of streamwise velocity along the centreline after $x \approx 3D$ is apparent, as the flow transitions from a laminar, jet-like velocity profile to a more uniform turbulent profile, as a result of which the velocity close to the wall will rise. The region of the turbulent spot is coincident with streamwise velocity fluctuations that increase in intensity close to the trailing edge of the spot. After $x \approx 12D$, the fluctuation levels drop and centreline velocity tends towards its asymptotic value of 2.0. This is contrast to the axisymmetric model in which centreline velocities are higher than their upstream value even as far downstream as $x = 22D$. Motivated by a recent study of spatially localized structures in pipe flow (Priymak & Miyazaki 2004), we compared these results with those associated with a turbulent 'puff'. Puffs were first reported by Wygnanski & Champagne (1973) and Wygnanski, Sokolov & Friedman (1975) in their early investigations of pipe flow transition at Reynolds numbers between 2000 and 2700. A characteristic trace of streamwise velocity along the pipe centreline, corresponding to the location of a puff, obtained by Wygnanski *et al.* (1975) at a transitional Reynolds number close to 2400 is shown in figure 17(*b*). The gradual velocity drop along the leading edge of the puff, followed by increasing turbulence intensity in the interior, closely resembles the velocity traces for the eccentric case. However, the trailing interface of the spot formed in the current simulations is not as distinct as in a typical puff, with the sharp growth in velocity at the trailing edge of the puff, as it regains its normal laminar value, not quite as visible in figure 17(*a*). Instead, there is an engulfment of laminar and turbulent fluid after $x \approx 11D$. Note that the comparison between traces is strictly qualitative since the experimental data are a time record whereas the numerical data correspond to a spatial distribution of instantaneous streamwise velocity along the vessel centreline.

The λ_2 structures in figure 15 also indicate the presence of weak streamwise structures in this region, which contribute to this mixing process as relaminarization progresses. However, centreline velocities in the region beyond $x = 12D$, downstream of the turbulent spot, are lower than their laminar counterparts, indicating that complete relaminarization does not occur within the length of the vessel considered in this study.

3.3. *Wall shear stress*

Figure 18 shows axial wall shear stress (WSS) variations across the vessel walls for the axisymmetric and eccentric models at $Re = 500$ and 1000. The circumferential locations at which shear stresses were obtained are also indicated in the figure. WSS across the vessel has been scaled by its value upstream of the stenosis, close to the inlet region. As the figure shows, WSS profiles for the two stenosis models are identical till about $x = 1D$. At $Re = 500$, WSS rises by more than a factor of 30 immediately prior to the throat. At the throat itself, $x = 0D$, WSS is about 22 times upstream levels. These results compare reasonably to the measurements of Ahmed & Giddens (1983*a*), who found WSS at the throat to exceed upstream levels by a factor of 24. At the higher Reynolds number of 1000, WSS increases by more than a factor of 40 close to the throat.

Shear stress levels drop significantly and return to their upstream levels within the diverging section of the stenosis, before becoming negative as flow separation takes place. The asymmetric post-stenotic flow field in the eccentric model results in WSS profiles for this model departing quite significantly from their axisymmetric counterpart in the region $x \geqslant 1D$. In the axisymmetric model, WSS is negative until flow reattachment occurs at $x \approx 11D$ for the $Re = 500$ case, whereas axial stresses

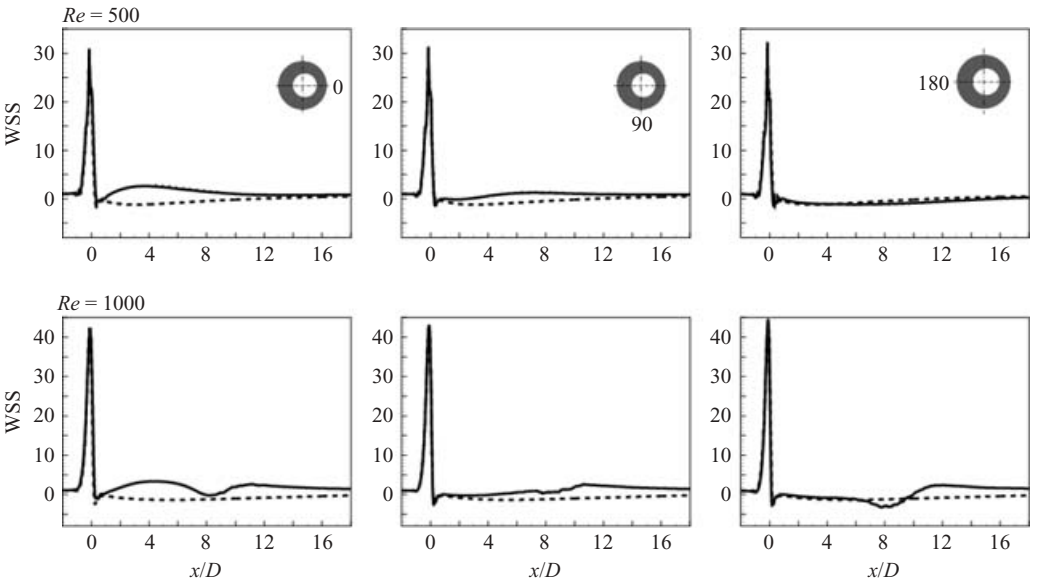

FIGURE 18. Axial wall shear stress, normalized by the value upstream of the stenosis, for steady flow through the 75 % axisymmetric (dashed line) and eccentric (solid line) stenosis models at $Re = 500$ and 1000. WSS for the eccentric case at $Re = 1000$ is time-averaged. The circumferential locations at which WSS was obtained are also indicated.

remain negative throughout the entire downstream section at $Re = 1000$. As we saw in § 3.2, the flow field downstream of the eccentric stenosis is laminar at $Re = 500$, but asymmetric. The deflection of the jet towards the side of the eccentricity results in high WSS along this side, attaining a maximum of up to twice upstream values at $x \approx 3D$, and low negative stresses coinciding with flow separation on the opposite side. In the far downstream region, $x \geqslant 14D$, shear levels for the two stenosis models at the lower Reynolds number are almost identical, but still slightly lower than upstream levels.

Time-averaged WSS for the eccentric model at $Re = 1000$ is qualitatively similar to the lower Reynolds number case till $x \approx 6D$, with stenotic jet deflection resulting in high shear stresses along the side with the eccentricity and negative stresses on the other side. However, transition to turbulence after this location results in a drop in axial shear stress. At $x \approx 8D$ WSS drops to less than -3, lower than corresponding WSS levels for the laminar axisymmetric case. Shear levels increase close to the trailing edge of the turbulent spot ($x \approx 10D$), after which they are close to upstream levels. This is in contrast to the corresponding axisymmetric case, in which shear stresses are lower than upstream levels even in the far downstream region, a result of the laminar post-stenotic flow field failing to reattach.

The instantaneous axial WSS distribution in the region $1D \leqslant x \leqslant 15D$ is shown in figure 19. In contrast to time-averaged results, which showed relatively low shear levels in the turbulent region, instantaneous axial shear stress magnitudes between $x = 8D$ and $11D$ rise by more than a factor of ten from upstream levels. Maximum and minimum values are close to 16 and -8 respectively. Significant axial and circumferential WSS gradients occur as a result of transition to turbulence, reducing only after $x \approx 11D$ when the relaminarization process starts to take over. Instantaneous axial shear stress levels can be seen to return close to upstream levels in the region $x \geqslant 14D$ (≈ 1.0).

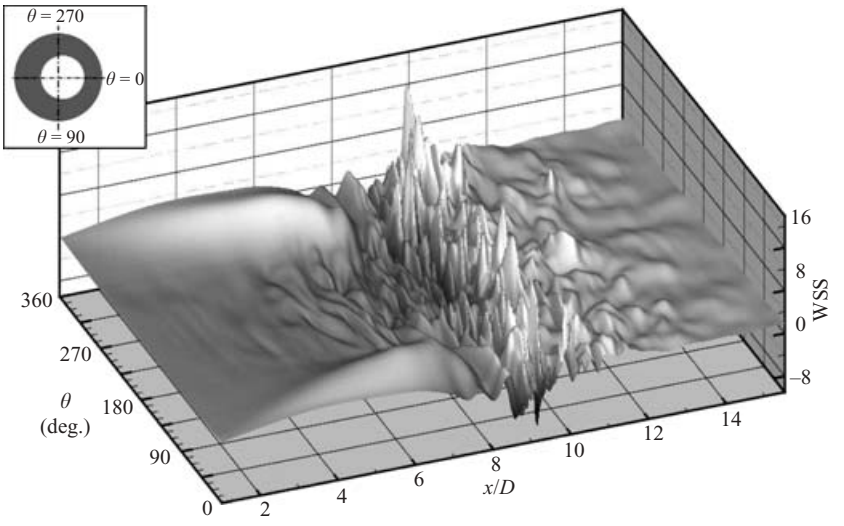

FIGURE 19. Instantaneous axial wall shear stress in the post-stenotic region $1D \leqslant x \leqslant 15D$, highlighting the axial and circumferential distribution for steady flow through the 75 % eccentric stenosis at $Re = 1000$. WSS has been normalized by its value upstream of the stenosis.

3.4. *Comparison with previous studies*

In the case of the axisymmetric stenosis, the simulations predict a completely stable and axisymmetric post-stenotic flow field at both $Re = 500$ and 1000. A simulation at $Re = 750$ was also performed to directly compare with data presented by Sherwin & Blackburn (2005), who used a similar axisymmetric stenosis model configuration for their numerical simulations. The post-stenotic flow field in this case was also predicted to be stable and axisymmetric (not presented here), with reattachment occurring soon after $x = 16D$, which matches almost exactly with the $x \approx 16.2D$ location they predicted. The results obtained in our study are unlike the observations made by Ahmed & Giddens (1983*a*, *b*) in their experiments, in which the post-stenotic region was completely laminar only at $Re = 250$. As the Reynolds number was increased to 500, they observed that the shear layer exhibited periodic discrete-frequency oscillations near the trailing edge of the recirculation region. At $Re = 1000$, vortex shedding at a discrete frequency was observed before $x = 4D$, after which the flow transitioned to turbulence. The occurrence of transition downstream of the shear layer can result in a shifting of the reattachment point from that observed for a purely laminar flow field. This may explain the differences between the computed and measured velocity profiles at $Re = 500$, shown in figure 7, especially at downstream locations close to the experimental reattachment zone, $4D \leqslant x \leqslant 6D$. The experimental profiles in this region exhibit increased bluntness, while their computed counterparts maintain a jet-like character throughout. In general, as the Reynolds number increases, the transition region tends to move upstream, with the reattachment zone no longer as well defined as at lower Reynolds numbers. This phenomenon was clearly evident in our eccentric model simulations at $Re = 1000$, when transition to turbulence resulted in early flow reattachment. At $Re = 1000$, Ahmed & Giddens (1983 *b*) observed discrete-frequency vortex shedding at $x = 2.5D$ and intense turbulence (with u_{rms}/u_i exceeding 70 %) in the shear layer at $x = 4D$, a post-stenotic flow field quite different from the laminar flow field computed in this study at the same Reynolds number for the axisymmetric model.

The results obtained here are consistent with the recent stability analysis studies of steady and pulsatile axisymmetric stenotic flows by Sherwin & Blackburn (2005). They observed that flow undergoes a Coanda-type wall attachment with jet deflection away from the axis of symmetry when a small perturbation flow component is added to an unstable steady base flow. Following saturation of this combination, the flow undergoes local transition to turbulence at a critical Reynolds number of 688, with the onset of turbulent breakdown propagating up to $x \approx 4D$. As Sherwin & Blackburn suggest, the onset of turbulence in the experiments of Ahmed & Giddens (1983*b*) may have been triggered by instabilities arising from upstream noise, a factor that was absent in all the simulations reported here. At the suggestion of a reviewer, we conducted a separate set of simulations for the axisymmetric stenosis that included the addition of a swirl-like perturbation to the inlet velocity profile. The streamwise velocity was unchanged, as defined in equation (2.3), but non-zero cross-stream inflow velocity components were specified such that the maximum amplitude of this perturbation was only 2 % of the average inlet velocity (u_i). The simulations confirmed that at Reynolds numbers of 750 and 1000, upstream disturbances can result in localized transition in the post-stenotic flow field. Results obtained were similar to those presented by Sherwin & Blackburn (2005) and are omitted here since these computations were along the lines of their study. Our goal here is to show that a quantifiable and perfectly replicable geometric perturbation in the form of a small stenosis eccentricity can result in post-stenotic transition to turbulence, even in the absence of upstream disturbances.

As seen in § 3.2, an eccentricity of $0.05D$ at the stenosis throat was unable to trigger sustained disturbances, and the post-stenotic flow field remained laminar throughout at $Re = 500$. At the higher Reynolds number of 1000, however, the geometric perturbation resulted in the flow transitioning to turbulence after $x = 6D$, as demonstrated by turbulent statistics and broadband energy spectra presented in § 3.2.2 and § 3.2.3. In spite of the geometric variation between our eccentric stenosis and the experimental axisymmetric model, the behaviour of the flow in the post-stenotic region as it transitions to turbulence was markedly similar to the observations by Ahmed & Giddens (1983*a*) at the same Reynolds number. In both cases, as transition occurred, instabilities propagated along the shear layer, and turbulent energy was highest within it before being redistributed across the entire cross-section. The fact that transition to turbulence occurred earlier in the experiments, at $x = 4D$, could perhaps be attributed to instabilities arising from upstream noise, as opposed to a geometric asymmetry.

With the same axisymmetric model, Ahmed & Giddens (1983*a*) measured the normalized centreline energy spectrum of streamwise velocity fluctuations, u', similar to the computed spectra presented in the previous section. The experimentalists found that at $x = 1.5D$, the spectrum displayed a narrow peak at $N_s = 4.2$ followed by a broader peak at $N_s = 2.3$ farther downstream at $x = 2.5D$. Spectra at $x = 4D$ and $6D$ were characteristic of broadband turbulence, with no evidence of discrete-frequency phenomena. The spectra shown in figure 14 for the eccentric case at $Re = 1000$ are consistent with these results in that the spectral peak at $x = 2D$ is at $N_s = 3.3$ and it shifts downward to about $N_s = 3.0$ at $x = 4D$ before dispersing into broadband spectra farther downstream. Also, the intensity of the spectral peak increased with axial distance, indicating more energy transfer into the starting vortex structure.

In an earlier study, Cassanova & Giddens (1978) analysed flow fields downstream of both sharp-edged and axisymmetric contoured occlusions of varying degrees. The latter was generated by intersecting circular arcs, unlike the cosine wave used to generate the smooth stenosis in this study. For steady inlet flow at $Re = 635$, with a

plug-shaped inlet velocity profile rather than a fully developed one, they observed that the 75 % sharp-edged occlusion produced a set of small vortices that disintegrated before the stenotic jet expanded to meet the wall. However, the contoured occlusion produced a large-scale flow instability downstream of the stenosis, which appeared to break up upon interaction with the tube wall at the reattachment location, quite similar to the large streamwise structure that broke down into small-scale structures close to the reattachment zone at $Re = 1000$ in our eccentric model. Non-dimensional energy spectrum correlations by the experimentalists indicated that the contoured occlusion showed spectral peaks at Strouhal numbers ($St = fd/u_j$) in the range 0.5–0.6 at axial locations between $x = 1D$ and $3.125D$. The current results match these correlations well, with the spectral peaks in figure 14 occurring between $fd/u_j = 0.53$ and 0.48 at axial locations $x = 2D$ and $4D$, respectively.

4. Conclusions

Direct numerical simulations of steady flow through smoothly contoured stenosed tubes with a maximum area reduction of 75 % have been carried out. At inlet Reynolds numbers of 500 and 1000, DNS predicts a laminar flow field downstream of an axisymmetric stenosis model. At $Re = 500$, the numerics agree with previous experimental measurements immediately downstream of the stenosis, but further downstream, after about four vessel diameters from the stenosis throat ($x \approx 4D$), the experiments recorded disturbed flow (with transition to turbulence occurring at $Re = 1000$) and consequently, early reattachment.

Symmetry breaking in our study was accomplished via a geometric perturbation in the form of a stenosis eccentricity, 5 % of the main vessel diameter at the throat, a relevant addition in that real-life stenoses are more likely to be eccentric rather than axisymmetric. Stenosis eccentricity causes the jet to deflect towards the side of the eccentricity, but at $Re = 500$, the flow remained laminar. However, at a high enough inlet Reynolds number of 1000, jet breakdown occurred and the post-stenotic flow field transitioned to localized turbulence. Low-frequency vortex shedding, indicated by velocity spectra, was found to take place in the region between the throat and $x = 4D$, with more energy transfer into the vortices as the distance from the stenosis increased, the results matching well with experimental spectral correlations. Turbulence statistics indicated the presence of streamwise velocity fluctuations in this immediate downstream region but these are most likely to be due to the wave-like motion of the stenotic jet, rather than turbulence. The lack of coherent structures and turbulent kinetic energy at these locations supports this conclusion. As flow transitioned into turbulence after $x \approx 5D$, the spectra started to take on a more broadband nature, achieving a $-5/3$ slope that is typical of turbulent flows. The transition process was accompanied by streamwise vortices that broke up to form a localized turbulent spot with large r.m.s. velocity and turbulent energy levels. The turbulent spot, qualitatively similar to turbulent puffs observed in pipe flow transition, was found to occupy the entire vessel cross-section between $x \approx 9D$ and $12D$, downstream of which the turbulent fluctuations and energy levels rapidly decayed and flow relaminarized. Broadband spectra confirmed that the flow within the spot was indeed turbulent.

Wall shear stress magnitudes at the stenosis throat were found to exceed upstream levels by more than a factor of 30. The immediate post-stenotic section was characterized by low WSS levels, as a result of flow separation along the vessel walls. Transition to turbulence in the case of the eccentric stenosis model was manifested in large temporal and spatial (both axial and circumferential) variations in instantaneous

WSS levels, rising by more than a factor of ten from upstream levels within the turbulent region. Time-averaged axial shear stress magnitudes within the turbulent zone were almost three times higher than those found upstream of the stenosis.

The detailed analysis presented here, of steady flow through idealized stenosis models, at physiologically relevant Reynolds numbers, provides a fundamental understanding of the complex flow field that may arise downstream of a clinically significant stenosis, as well as its impact on an important haemodynamic parameter such as wall shear stress. The steady flow analysis also serves as a suitable precursor to analysing the more physiologically realistic pulsatile flow. As Part 2 of this study (Varghese *et al.* 2007) will go on to show, the flow features arising as a result of a stenosis, such as separation, reattachment, recirculation and strong shear layers, as observed here, combine with flow pulsatility to produce periodic transition to turbulence and subsequent relaminarization of post-stenotic flow.

This work was supported in part by the Mathematical, Information, and Computational Sciences Division subprogram of the office of Advanced Scientific Computing Research, Office of Science, US Department of Energy, under Contract DE-AC02-06CH11357.

REFERENCES

Abdallah, S. A. & Hwang, N. H. C. 1988 Arterial stenosis murmurs: An analysis of flow and pressure fields. *J. Acoust. Soc. Am.* **83**, 318–334.

Ahmed, S. A. & Giddens, D. P. 1983*a* Velocity measurements in steady flow through axisymmetric stenoses at moderate Reynolds number. *J. Biomech.* **16**, 505–516.

Ahmed, S. A. & Giddens, D. P. 1983*b* Flow disturbance measurements through a constricted tube at moderate Reynolds numbers. *J. Biomech.* **16**, 955–963.

Ahmed, S. A. & Giddens, D. P. 1984 Pulsatile poststenotic flow studies with laser Doppler anemometry. *J. Biomech.* **17**, 695–705.

Bathe, M. & Kamm, R. 1999 A fluid- structure interaction finite element analysis of pulsatile blood flow through a compliant stenotic artery. *J. Biomech. Engng* **121**, 361–369.

Berger, S. & Jou, L.-D. 2000 Flows in stenotic vessels. *Annu. Rev. Fluid Mech.* **32**, 347–382.

Buchanan Jr., J., Kleinstreuer, C. & Comer, J. 2000 Rheological effects on pulsatile hemodynamics in a stenosed tube. *Computers Fluids* **29**, 695–724.

Cassanova, R. A. & Giddens, D. P. 1978 Disorder distal to modeled stenoses in steady and pulsatile flow. *J. Biomech.* **11**, 441–453.

Clark, C. 1980 The propagation of turbulence produced by a stenosis. *J. Biomech.* **13**, 591–604.

Deshpande, M. D. & Giddens, D. P. 1980 Turbulence measurements in a constricted tube. *J. Fluid Mech.* **97**, 65–89.

Deville, M. O., Fischer, P. F. & Mund, E. H. 2002 *High-Order Methods for Incompressible Fluid Flow*. Cambridge University Press.

Eliahou, S., Tumin, A. & Wygnanski, I. 1998 Laminar-turbulent transition in Poiseuille pipe flow subjected to periodic perturbation emanating from the wall. *J. Fluid Mech.* **361**, 333–349.

Fischer, P. F. 1997 An overlapping Schwarz method for spectral element solution of the incompressible Navier-Stokes equations. *J. Comput. Phys.* **133**, 84–101.

Fischer, P. F., Kruse, G. & Loth, F. 2002 Spectral element methods for transitional flows in complex geometries. *J. Sci. Comput.* **17**, 81–98.

Fischer, P. F. & Mullen, J. 2001 Filter-based stabilization of spectral element methods. *C. R. l'Acad. Sci. Paris* I **332**, 265–270.

Fredberg, J. J. 1974 Origin and character of vascular murmurs: Model studies. *J. Acoust. Soc. Am.* **61**, 1077–1085.

Han, G., Tumin, A. & Wygnanski, I. 2000 Laminar-turbulent transition in Poiseuille pipe flow subjected to periodic perturbation emanating from the wall. Part 2. Late stage of transition. *J. Fluid Mech.* **419**, 1–27.

He, S. & Jackson, J. 2000 A study of turbulence under conditions of transient flow in a pipe. *J. Fluid Mech.* **408**, 1–38.

Hinze, J. O. 1975 *Turbulence*. McGraw-Hill.

Jeong, J. & Hussain, F. 1995 On the identification of a vortex. *J. Fluid Mech.* **285**, 69–94.

Khalifa, A. M. A. & Giddens, D. P. 1981 Characterization and evolution of post-stenotic flow disturbances. *J. Biomech.* **14**, 279–296.

Kim, B. M. & Corcoran, W. H. 1974 Experimental measurements of turbulence spectra distal to stenoses. *J. Biomech.* **7**, 335–342.

Klebanoff, P. S., Tidstrom, K. D. & Sargent, L. M. 1962 The three-dimensional nature of boundary layer instability. *J. Fluid Mech.* **12**, 1–34.

Ku, D. N. 1997 Blood flow in arteries. *Annu. Rev. Fluid Mech.* **29**, 399–434.

Lieber, B. B. & Giddens, D. P. 1988 Apparent stresses in disturbed pulsatile flows. *J. Biomech.* **21**, 287–298.

Lieber, B. B. & Giddens, D. P. 1990 Post-stenotic core flow behavior in pulsatile flow and its effects on wall shear stress. *J. Biomech.* **23**, 597–605.

Lu, P. C., Gross, D. R. & Hwang, N. H. C. 1980 Intravascular pressure and velocity fluctuations in pulmonic arterial stenosis. *J. Biomech.* **13**, 291–300.

Lu, P. C., Hui, C. N. & Hwang, N. H. C. 1983 A model investigation of the velocity and pressure spectra in vascular murmurs. *J. Biomech.* **16**, 923–931.

Lusis, A. J. 2000 Atherosclerosis. *Nature* **407**, 233–241.

Maday, Y., Patera, A. T. & Rønquist, E. M. 1990 An operator-integration-factor splitting method for time-dependent problems: Application to incompressible fluid flow. *J. Sci. Comput.* **5**, 263–292.

Mallinger, F. & Drikakis, D. 2002 Instability in three-dimensional unsteady stenotic flows. *Intl J. Heat Fluid Flow* **23**, 657–663.

Mittal, R., Simmons, S. P. & Najjar, F. 2003 Numerical study of pulsatile flow in a constricted channel. *J. Fluid Mech.* **485**, 337–378.

Ojha, M., Cobbold, C., Johnston, K. & Hummel, R. 1989 Pulsatile flow through constricted tubes: An experimental investigation using photochromic tracer methods. *J. Fluid Mech.* **13**, 173–197.

Priymak, V. G. & Miyazaki, T. 2004 Direct numerical simulation of equilibrium spatially localized structures in pipe flow. *Phys. Fluids* **16**, 4221–4234.

Ryval, J., Straatman, A. G. & Steinman, D. A. 2004 Two-equation turbulence modeling of pulsatile flow in a stenosed tube. *J. Biomech. Engng* **126**, 625–635.

Scotti, A. & Piomelli, U. 2001*a* Numerical simulation of pulsating turbulent channel flow. *Phys. Fluids* **13**, 1367–1384.

Scotti, A. & Piomelli, U. 2001*b* Turbulence models in pulsating flow. *AIAA Paper* 01-0729.

Shan, H., Ma, B., Zhang, Z. & Nieuwstadt, F. T. M. 1999 Direct numerical simulation of a puff and a slug in transitional cylindrical pipe flow. *J. Fluid Mech.* **387**, 39–60.

Sherwin, S. J. & Blackburn, H. M. 2005 Three-dimensional instabilities and transition of steady and pulsatile axisymmetric stenotic flows. *J. Fluid Mech.* **533**, 297–327.

Stroud, J., Berger, S. & Saloner, D. 2000 Influence of stenosis morphology on flow through severely stenotic vessels: Implications for plaque rupture. *J. Biomech.* **33**, 443–455.

Tang, D., Yang, J., Yang, C. & Ku, D. 1999 A nonlinear axisymmetric model with fluid-wall interactions for steady viscous flow in stenotic elastic tubes. *J. Biomech. Engng* **121**, 494–501.

Tennekes, H. & Lumley, J. L. 1972 *A First Course in Turbulence*. MIT Press.

Varghese, S. S. & Frankel, S. H. 2003 Numerical modeling of pulsatile turbulent flow in stenotic vessels. *J. Biomech. Engng* **125**, 445–460.

Varghese, S. S., Frankel, S. H. & Fischer, P. F. 2007 Direct numerical simulation of stenotic flows. Part 2. Pulsatile flow. *J. Fluid Mech.* **582**, 281–318.

Welch, P. D. 1967 The use of fast Fourier transform for the estimation of power spectra: A method based on time averaging over short modified periodograms. *IEEE Trans. Audio Electroacousti.* AU **15**, 70–73.

Wilcox, D. 1993 *Turbulence Modeling for CFD*. La Cañada, California, CA: DCW Industries.

Winter, D. C. & Nerem, R. M. 1984 Turbulence in pulsatile flows. *Ann. Biomed. Engng* **12**, 357–369.

Womersley, J. R. 1955 Method for the calculation of velocity, rate of flow and viscous drag in arteries when the pressure gradient is known. *J. Physiol.* **127**, 553–563.

Wootton, D. M. & Ku, D. N. 1999 Fluid mechanics of vascular systems, diseases, and thrombosis. *Annu. Rev. Biomed. Engng* **1**, 299–329.

Wygnanski, I. J. & Champagne, F. H. 1973 On transition in a pipe. Part 1. The origin of puffs and slugs and the flow in a turbulent slug. *J. Fluid Mech.* **59**, 281–335.

Wygnanski, I. J., Sokolov, M. & Friedman, D. 1975 On transition in a pipe. Part 2. The equilibrium puff. *J. Fluid Mech.* **69**, 283–304.

Young, D. F. 1979 Fluid mechanics of arterial stenosis. *J. Biomech. Engng* **101**, 157–173.

Young, D. F. & Tsai, F. Y. 1979*a* Flow characteristics in models of arterial stenoses – I steady flow. *J. Biomech. Engng* **6**, 395–410.

Young, D. F. & Tsai, F. Y. 1979*b* Flow characteristics in models of arterial stenoses – II unsteady flow. *J. Biomech. Engng* **6**, 547–559.